# Evaluating Soil Water Content in a WRF-Noah Downscaling Experiment

PETER GREVE,* KIRSTEN WARRACH-SAGI, AND VOLKER WULFMEYER

*Institute of Physics and Meteorology, University of Hohenheim, Stuttgart, Germany*

(Manuscript received 5 September 2012, in final form 26 April 2013)

ABSTRACT

Soil water content (SWC) depends on and affects the energy flux partitioning at the land–atmosphere interface. Above all, the latent heat flux is limited by the SWC of the root zone on one hand and radiation on the other. Therefore, SWC is a key variable in the climate system. In this study, the performance of the Weather Research and Forecasting model coupled with the Noah land surface model (WRF-Noah) system in a climate hindcast simulation from 1990 to 2008 is evaluated with respect to SWC versus two reanalysis datasets for Europe during 2007 and 2008 with in situ soil moisture observations from southern France. When compared with the in situ observations, WRF-Noah generally reproduces the SWC annual cycle while the reanalysis SWCs do not. The biases in areal mean WRF-Noah SWCs relate to biases in precipitation and evapotranspiration in a cropland environment. The spatial patterns and temporal variability of the seasonal mean SWCs from the WRF-Noah simulations and from the two reanalyses correspond well, while absolute values differ significantly, especially at the regional scale.

## 1. Introduction

The land surface is a key factor within the climate system, contributing to a large variety of different processes. The soil texture and the amount of water within the soil play a key role in the exchange of moisture and heat between the atmosphere and the land surface by influencing evapotranspiration (ET). Some 1.7% of the total water and 31% of the earth's freshwater are stored within the soil.

The amount of soil water induces several feedbacks within the weather and climate system. Most important, due to the link between evapotranspiration and soil water, the structure and stability of the atmospheric boundary layer is influenced. This can lead to a modification of clouds and precipitation. However, detecting the strength and sign of this feedback process is still subject to research in climate science. Most studies indicate a positive feedback caused by wet soils leading to more precipitation-trough-enhanced evapotranspiration (Yeh et al. 1984; Beljaars et al. 1996; Eltahir 1998; Schär et al. 1999). Other studies indicate a positive feedback through enhanced instability within the planetary boundary layer (Ek and Mahrt 1994; Taylor and Ellis 2006; Alfieri et al. 2008). Nevertheless, some studies showed that dry soils could also induce near-surface instability and thus more precipitation, indicating a negative feedback (Findell and Eltahir 2003; Koster et al. 2004; Hohenegger et al. 2009; Gantner and Kalthoff 2010) by shifting the planetary boundary layer height toward higher values, which would thus favor the initiation of convection. Feedbacks between the land surface and the atmosphere were also considered by Ek and Holtslag (2004), Santanello et al. (2007), Heerwaarden et al. (2009), and Seneviratne et al. (2010). For instance, Santanello et al. (2007) introduced a technique for studying land surface variables in combination with key variables in the convective atmospheric boundary layer such as moisture and entrainment flux. They demonstrated that feedback regimes can be derived such as soil moisture–limited and soil moisture–saturated cases.

The coupling between temperature and soil water anomalies has been studied in detail within the last decade. Dry soil anomalies likely lead to a significant increase in extreme hot days (Clark et al. 2006; Seneviratne et al. 2006; Hirschi et al. 2010). These studies show that latent heat flux decreases under soil-water-limited conditions because transpiration is constrained in dry soils.

Denotes Open Access content.

* Current affiliation: Institute for Atmospheric and Climate Science, ETH Zürich, Zürich, Switzerland.

*Corresponding author address:* Peter Greve, Institute for Atmospheric and Climate Science, ETH Zürich, Universitätsstrasse 16, Zürich 8092, Switzerland.
E-mail: peter.greve@env.ethz.ch

DOI: 10.1175/JAMC-D-12-0239.1

Sensible heat flux, as another part of the energy balance, is thus enhanced, leading to higher temperatures. This mechanism, for example, influenced the strength of the 2003 European summer heat wave (Beniston 2004; Black et al. 2004; Fischer et al. 2007). Negative soil water anomalies also increase the persistence of heat waves, due to the longevity of the soil water anomalies (Lorenz et al. 2010).

The impact of soil water on precipitation is also important on shorter time scales for numerical weather prediction (NWP) from nowcasting to the medium range. This issue was pointed out by observing precipitation processes with most modern remote sensing research systems during the Convective and Orographically-Induced Precipitation Study (COPS) field campaign in southwest Germany (Wulfmeyer et al. 2011). Within the COPS framework, the high dependence of initial soil water fields on convective processes and atmospheric stability was especially underlined in Kalthoff et al. (2011), Hauck et al. (2011), and Barthlott et al. (2011). Significant influences on surface energy balance components were found, when altering the initial soil moisture fields. Impacts on convective indices and precipitation were identified as being evident, but asymmetric, due to various complex processes interacting. It is important to confirm these effects by more extensive field studies and by their coordination with extensive modeling studies.

State-of-the-art land surface models (LSMs) capture the most important features of soil hydrology and are coupled to the atmospheric model via the surface energy balance, the surface layer stability, and the water balance equation. In this study, a regional hindcast climate simulation was performed using version 3.1 of the Noah LSM coupled to the Weather Research and Forecasting (WRF) model. Latent heat flux and evapotranspiration, respectively, are limited by the soil water content in the root zone and the available energy. Since this therefore impacts the energy flux partitioning at the lower atmospheric boundary, soil water content is a key component to be evaluated in climate simulations. As no physiological and biological modules are included, this version of the Noah model could be classified as a second-generation LSM (Sellers et al. 1997). For the purposes of this climate simulation we investigate whether the use of a second-generation LSM is sufficient and whether the main characteristics of soil hydrology are well presented and could possibly be improved by using physically based dynamical downscaling. This is an area of great interest in our ongoing research into feedbacks and land–atmosphere coupling. Additionally, a good treatment of soil moisture in climate models is important for many topics ranging from hydrological (groundwater renewal, future flooding statistics for protection of the environment), agricultural applications (yield and yield quality), and matter transport (environmental protection) in the era of climate change.

These concepts are examined by comparing WRF-Noah to in situ observations of soil moisture in southern France (section 4a) as well as to two reanalysis datasets (section 4b). One of the reanalysis datasets employed a first-generation LSM, the other a second-generation LSM, comparable to Noah. The WRF-Noah model setup is described in section 2. Further details on the data are given in section 3. The findings are discussed in section 5, followed by a summary and our conclusions in section 6.

## 2. The WRF-Noah model system

The Advanced Research core of the WRF model, version 3.1.0, is run in with the Noah LSM for a hindcast evaluation covering the period from 1989 to 2008. WRF is a compressible, nonhydrostatic, mesoscale model using a terrain-following vertical coordinate (Skamarock et al. 2008). WRF-Noah was operated over Europe on a rotated latitude–longitude grid with a horizontal resolution of 0.11° and with 50 vertical layers up to 20 hPa with a time step of 30 s. Driven by European Centre for Medium-Range Weather Forecasts (ECMWF) Interim Re-Analysis (ERA-Interim) forcing data (Dee et al. 2011) at the boundaries (available at approximately 0.75°), WRF-Noah dynamically downscales this data first to 0.33° in an outer surrounding domain and second to 0.11°, following the study of Heikkilä et al. (2011). Results concerning precipitation statistics are presented and discussed in Warrach-Sagi et al. (2013).

From experience with previous applications of WRF in central Europe in weather forecast mode (Schwitalla et al. 2011), it was decided to use the Morrison two-moment microphysics scheme (Morrison et al. 2009), and the Yonsei University atmospheric boundary layer parameterization (Hong et al. 2006). Further, the Kain–Fritsch Eta Model convection scheme (Kain 2004) and the Community Atmosphere Model shortwave and longwave radiation schemes (Collins et al. 2004) were chosen.

WRF-Noah applies global datasets for land cover classes and soil texture. The vegetation maps are based on the slightly modified version of the Boston University–International Geosphere–Biosphere Programme (IGBP) land cover classification based on data from the Moderate Resolution Imaging Spectroradiometer (MODIS) with four additional classes of tundra and shrubland vegetation. Noah includes a monthly climatology of the vegetation fraction. Soil texture is divided into 16 soil categories, based on the Food and Agriculture Organization of the United Nations soil dataset with a spatial resolution over Europe of 5′. All parameters are

interpolated with the WRF preprocessor onto the 0.11°-resolution WRF-Noah model.

An LSM calculates water and energy fluxes within the soil and at the land–atmosphere interface. The Noah LSM can either be operated offline or coupled with an atmospheric model. Here, WRF-Noah results are presented and discussed. Atmospheric variables are passed from the lowest model level of WRF to Noah. A detailed description is given in Chen and Dudhia (2001). The model consists of four soil layers, with thicknesses of 10, 30, 60, and 100 cm (giving a total of 2 m). Both, volumetric soil water content and soil temperature are calculated in every layer.

The volume of soil water relative to the total volume (soil + water + air) is defined as the soil wetness $\theta$ ($m^3\,m^{-3}$). Noah calculates the soil wetness $\theta$ from the diffusive form of Richard's equation,

$$\frac{\partial\theta}{\partial t} = \frac{\partial}{\partial z}\left(D\frac{\partial\theta}{\partial z} + K\right) + F_\theta, \tag{1}$$

for each soil layer. The hydraulic conductivity $K$ and diffusivity $D$ depend on soil texture, and $F_\theta$ denotes additional sources and sinks of water. These are the precipitation not intercepted by the canopy, leaf drip, runoff, evapotranspiration, and root water uptake. SWC (mm) is used and is defined as the total height of the water within a certain soil column, $z_s$. Soil wetness and SWC are related as follows: $\theta = z_w/z_s$, with $z_w$ as the height of all water in a predefined soil column of height $z_s$. SWC of the upper 1.6 m is used as the quantity to evaluate WRF-Noah against the reanalysis data.

Simultaneously, the evolution of the soil temperature is calculated by solving the thermal diffusion equation:

$$C(\theta)\frac{\partial T}{\partial t} = \frac{\partial}{\partial z}\left[K_T(\theta)\frac{\partial T}{\partial z}\right]. \tag{2}$$

Equation (2) demonstrates the strong coupling between the land surface temperature and soil wetness, with $C$ being the volumetric heat capacity, $T$ the temperature, and $K_T$ the thermal conductivity. The fluxes and the skin temperature of the land are calculated by solving the energy balance closure (EBC) based on Mahrt and Ek (1984). This closure yields the potential evapotranspiration $E_p$, which is a function of radiative and soil heat fluxes as well as the bulk latent heat flux corrected for atmospheric stability. Evapotranspiration is calculated as the sum of the direct evaporation $E_{\mathrm{dir}}$ of the bare soil surface, evaporation of water intercepted by vegetation cover $E_c$, and transpiration of plants $E_t$, and all are all functions of soil wetness. Values of the canopy resistance $r_c$ are calculated from the leaf area index (LAI) and the weighting terms of solar radiation, water vapor pressure deficit, temperature differences, and soil wetness. The amount of water infiltrating into the soil depends on the soil texture and precipitation rate. Excess water leaves the surface as runoff. Snow coverage is treated as a single-layer accumulation model, resolving melting, sublimation, and heat exchange between the snow and either the air above or the soil below. Consequently, the soil wetness is a result of complex feedback processes in the coupled land surface–vegetation atmosphere system. For further details see Chen and Dudhia (2001) and Ek et al. (2003).

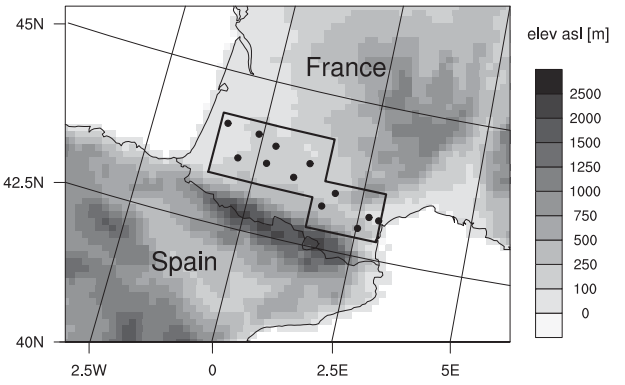


FIG. 1. The SM soil moisture network in southern France. The 12 stations (black dots) are located between the Gulf of Biscay and the Mediterranean. The irregular box shows the domain used to calculate areal means for WRF-Noah and ERA-I. The separation between the southeastern and northwestern parts is used to avoid effects of the Pyrenees in the south and the Massif Central in the north. Elevation data are from the WRF model at 0.11° resolution.

## 3. Evaluation data

The Soil Moisture Observing System (SMOS) Meteorological Automatic Network Integrated Application (SMOSMANIA, hereinafter SM) in situ observational dataset of soil wetness is used to perform an evaluation of Noah's sensitivity with respect to the land-the use index (LUI) and soil texture (Calvet et al. 2007; Albergel et al. 2008). Twelve stations measuring soil wetness at four depths (5, 10, 20, and 30 cm) with capacitance probes were installed in 2007 at existing weather stations in southern France between the Gulf of Biscay and the Mediterranean Sea to provide ground measurements for the validation of the SMOS satellite (see Fig. 1). The three most westward stations are located within the forest area of the Forêt des Landes, consisting mainly of Aleppo pines on sandy soils. The three most eastward stations are located within forests of Mediterranean type. The six stations in between have been installed within areas dominated by cropland (Albergel et al. 2008). As LUI

and soil texture in WRF-Noah reveal an equivalent picture, a direct comparison of station measurements to grid points classified with similar properties is possible.

Concerning SWC, the only measurements of the root zone available are from point measurements. In the past, simulations with land surface models forced with meteorological observations at the locations of the SWC measurements have shown an ability to capture the SWC even though they do not have a vertical soil texture profile and were set up with effective soil parameters (Warrach et al. 2001; Fan et al. 2006; Ingwersen et al. 2011). Applications of land surface models in river catchments with larger grid cells showed that these models are also able to simulate the runoff and streamflow when forced with observational meteorological data (Wood et al. 1998; Warrach-Sagi et al. 2008). Because of the heterogeneity of soil texture and vegetation within a model grid cell, point measurement data can only give an impression of the ability of the models to capture the SWC. The SWC is not expected to match exactly the model result at grid-box scale. Since the study area has 12 stations with different soil textures and vegetation types, their mean SWC and standard deviation give an impression of the variability and the annual cycle in the study area. When comparing the mean SWC from these measurements with the coupled atmosphere–land surface model data, the goodness of fit between the root zone soil moisture bandwidth and the variability at different time scales can be seen.

To evaluate SWC simulated by WRF-Noah on a spatiotemporal basis over Europe, two global reanalysis datasets were chosen due to a lack of large-scale observational data for SWC: 1) the approximately 0.75°, 6-hourly ERA-Interim (ERA-I; Dee et al. 2011) dataset and 2) the 0.5°, monthly mean global Climate Prediction Center (CPC) reanalysis dataset (Van den Dool et al. 2003). For comparison and evaluation, ERA-I and WRF-Noah model output are transformed into units of SWC in the upper 1.6 m as in CPC. Both datasets were remapped onto the 0.11° rotated latitude–longitude grid of WRF-Noah by using bilinear interpolations.

ERA-I calculates SWC by applying the Tiled ECMWF Scheme for Surface Exchanges over Land (TESSEL; Viterbo and Beljaars 1995). TESSEL divides each grid box into respective fractions of either bare soil, low or high vegetation, snow beneath vegetation or freely exposed snow, and intercepted water. Four soil layers are assumed, but with different layer thicknesses than Noah (i.e., 0.07, 0.21, 0.72, and 1.89 m), adding up to a total of 2.89 m. One major difference from Noah is the use of a global uniform soil texture, with a porosity of $0.472\,m^3\,m^{-3}$, a wilting point of $0.171\,m^3\,m^{-3}$, and a field capacity of $0.323\,m^3\,m^{-3}$. TESSEL has 20 land-use classes. Snow is treated similarly to Noah as an extra single layer above the ground. SWC and soil temperature are corrected using analysis increments of humidity and temperature out of the data assimilation system (Mahfouf et al. 2000).

A monthly mean, global 0.5° soil moisture reanalysis dataset provided by the CPC (Van den Dool et al. 2003) is computed with a simple leaky bucket model in the tradition of Manabe and Bryan (1969), consisting of one layer reaching down to 1.6-m depth. Porosity is set to 0.47 and the maximum water content to 760 mm. SWC is generated by solving the land–water balance equation. Precipitation is taken from a global gauge-based analysis dataset and evaporation is calculated using Thornthwaite's equation.

## 4. Model evaluation

### *a. Comparison with in situ observations*

Shown in Fig. 2 are the averaged soil wetness time series of SM stations (blue) enclosed by the range of the corresponding standard deviation (shaded light blue). Gaps occur in cases where measurements that are missing at more than two stations. WRF-Noah and ERA-I time series (red and green) represent averages of the whole domain shown in Fig. 1. Soil wetness data measured at 5-cm depth are compared with Noah's first layer (and ERA-I's first layer). To evaluate the second layer of Noah (and ERA-I's second layer), which ranges from 10 to 40 cm, the mean of SM soil wetness at 20 and 30 cm is used.

The largest soil wetness is observed in late winter–spring. During late summer–autumn the soil wetness is lower in the upper soil, with high peaks extending to wetter values. Largest and lowest values rank near those of the field capacity and wilting point, showing that conditions during winter–spring are overall very wet and conditions during summer–autumn very dry. This is typical for near-Mediterranean regions. Conditions at 5-cm depth are slightly wetter then at 25-cm depth. Furthermore, apart from a very high correlation between both time series ($r = 0.97$, all statistical values given in this study are significant at the 5% level) and a comparable spatial standard deviation (nearly constant throughout the year and very small for ERA-I), the temporal standard deviation under near-surface conditions at 5-cm depth is much larger.

Correlations of WRF-Noah and ERA-I to SM are large: 0.84 and 0.83 at 5-cm depth and 0.8 and 0.79 at 25-cm depth, respectively. Between the two models, correlations rank lower at ~0.65 for both depths. However, the root-mean-square (RMS) deviation is $0.048\,m^3\,m^{-3}$ between WRF-Noah and SM and thus significantly lower than that between ERA-I and SM, at $0.072\,m^3\,m^{-3}$.

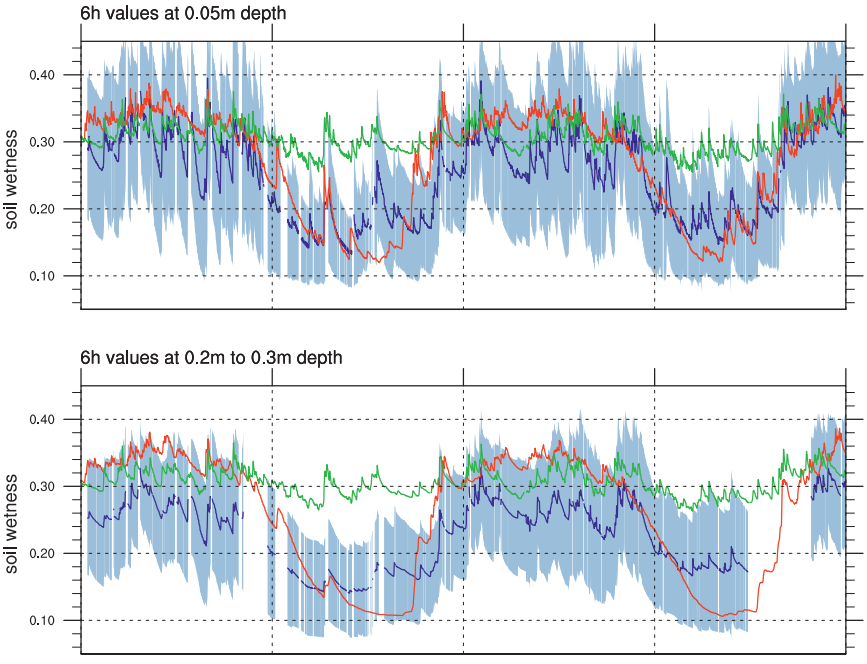


FIG. 2. Mean soil wetness and corresponding areal standard deviation (blue shading) of SM from at least 10 of 12 SM stations (blue), WRF-Noah (red), and ERA-I data (green) within the corresponding region at four time steps per day (0000, 0600, 1200, and 1800 UTC). Units are meters cubed per meters cubed. Depths taken into account are those corresponding to (top) the first layer of WRF-Noah (0.1 m) and (bottom) 0.2–0.3 m, which will represent the second layer of WRF-Noah (reaching from 0.1 to 0.4 m). Overall, the correlations of the model runs with the SM observations are high (0.83 for WRF-Noah and 0.84 for ERA-I).

During summer, the RMS of ERA-I is even larger ($0.108\,m^3\,m^{-3}$), whereas the WRF-Noah value is better ($0.041\,m^3\,m^{-3}$).

WRF-Noah is slightly wetter in winter–spring and in most cases is slightly drier in summer–autumn at 5-cm depth. ERA-I is comparable to SM in winter–spring but significantly wetter during summer–autumn, with values comparable to those under wet conditions. At 25 cm, WRF-Noah is wettest in the first half of the year, with a soil wetness being on average $0.1\,m^3\,m^{-3}$ larger then SM. In late summer and autumn, WRF-Noah is up to $0.08\,m^3\,m^{-3}$ drier than SM. ERA-I ranks between WRF-Noah and SM in winter–spring and is significantly ($0.15\,m^3\,m^{-3}$) wetter than SM in summer and autumn. The correlation between the time series from each model according to both layer depths is very large ($r > 0.95$).

A scatterplot, with SM being the reference, is shown in Fig. 3. At 0.05-m depth, the regression line of WRF-Noah (red line) has nearly the same slope (1.044) as the reference line of SM (blue line), but it is shifted $0.02\,m^3\,m^{-3}$ toward wetter values. The spread of WRF-Noah is rather large, with a standard deviation of the regression line of $0.014\,m^3\,m^{-3}$. The slope of ERA-I's regression line is fairly flat, with a value of 0.28. Furthermore, the spread of the ERA-I data points is much smaller than in WRF-Noah, resulting in a lower standard deviation of $0.004\,m^3\,m^{-3}$. At low soil wetness of SM, ERA-I is significantly larger. WRF-Noah is instead particularly drier then SM under dry conditions, except for some outliers, which are caused by precipitation simulated in WRF-Noah during autumn 2007, while no precipitation occurred at the SM stations. These outliers also cause an upward shift of the regression line, which would be much steeper otherwise. At values above $0.3\,m^3\,m^{-3}$, the differences get smaller, even for ERA-I, which coincides fairly well with SM under wet conditions. Two distinct accumulations appear in the wet and dry values, representing either wet conditions during winter–spring or dry conditions during summer–autumn. This bimodal structure is most distinct for SM.

At 0.25-m depth, some additional features are remarkable. Under wet conditions, ERA-I and WRF-Noah overestimate the soil wetness by approximately $0.1\,m^3\,m^{-3}$ on average.

Under dry conditions, most data points from the WRF-Noah simulation are located below the blue reference line of SM, indicating that WRF-Noah is drier. But as the transition between dry and wet soils in late

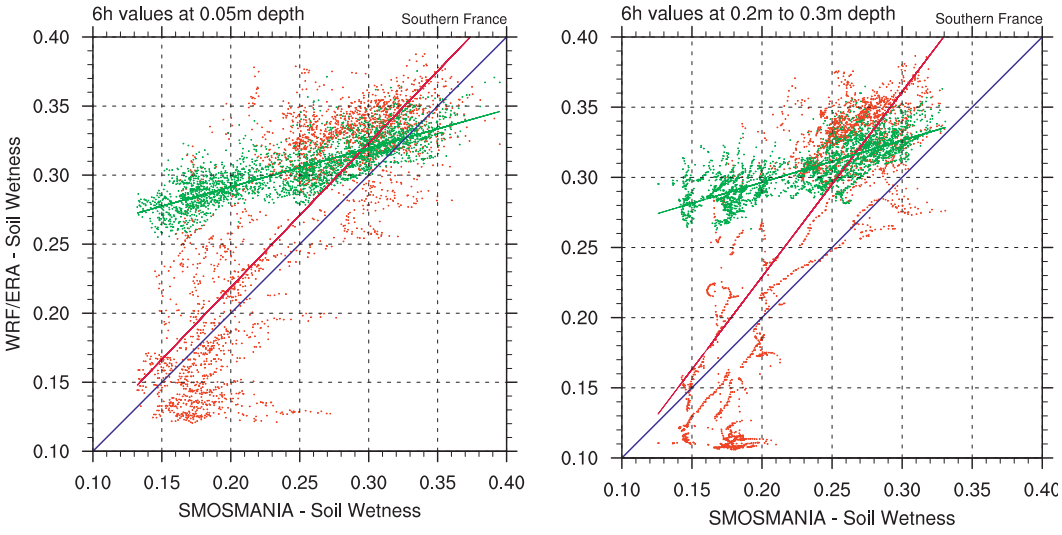


FIG. 3. Scatterplot of both WRF-Noah (red) and ERA-I (green) 6-h values within the SM region in southern France in comparison with the corresponding SM values, at (left) 0.05- and (right) 0.25 m depths. Units are meters cubed per meters cubed. The lines represent the associated regression lines. Note that all regression lines lie above the SM line (blue), indicating that both models are wetter than the measurements.

autumn begins a few weeks earlier than in SM, several outliers occur and shift the regression line once more to larger values. Nevertheless, due to significantly wetter conditions in winter–spring, the slope is now steeper (1.32). Because of nearly constant soil wetness occurring over long periods during summer, data points in WRF-Noah are no longer structured like a cloud, but rather follow certain lines. These lines have a more or less comparable slope to SM, revealing similar conditions during dry periods.

Results of a detailed analysis considering LUI and soil texture are shown in Fig. 4. The two most northwestern stations of SM located within Forêt des Landes are compared with spatial averages of those grid points in the underlying domain, which are classified as sand and evergreen needleleaf forest in WRF-Noah. Similarly, the six central stations compared with those grid points are classified as cropland and the two most eastward stations are compared with mixed forest grid points. Two stations are not considered due to their relatively high elevation and different soil properties.

The two SM stations within Forêt des Landes show high variability on very short time scales, associated with rain events. During dry periods in summer, soil wetness ranks below $0.1\,m^3\,m^{-3}$ because of low values of $\theta_f$ and $\theta_w$ (see Table 1). Under heavy rain conditions, soils get saturated, reaching values larger than $0.3\,m^3\,m^{-3}$. WRF-Noah does not represent this behavior completely. The correlation between the time series is very large. The variability on short time scales is smaller. However, the major characteristic of a very fast drainage back to low soil wetness after a sudden increase is not represented in a comparable way in WRF-Noah. Although the decline back to $\theta_f$ is similarly fast, the decrease toward $\theta_w$ is rather slow. The wilting point is thus never reached during persisting dry periods. WRF-Noah soil wetness is nearly twice as large at both depths in summer–early autumn, especially during 2007. The propagation of rain signals downward into deeper soil layers is underestimated in WRF-Noah. Very small high-frequency variability of the models in comparison with the observations at 25-cm depth may indicate this. WRF-Noah shows the largest variability on seasonal time scales reflecting the seasonal cycle, which is also visible in the observations, but less pronounced. ERA-I shows almost no seasonal variation and those variations corresponding to other time scales are rather small as well.

In a cropland environment, time series of the six SM stations show large variety. However, a seasonal cycle is visible for all stations and for WRF-Noah. For ERA-I this is not evident. For SM observations, high-frequency variability exceeds those of longer time scales. WRF-Noah behaves differently and generates weaker variability. Regarding the mean values, WRF-Noah fits fairly well with the observations in winter–spring and is drier in summer–autumn. ERA-I is too wet during summer–autumn.

Within a Mediterranean forest, sparse rain leads to a sudden increase in soil wetness above field capacity, followed by a nearly linear decline toward the wilting point. The wilting point is reached very fast and soil wetness remains at $\theta_w$ under persistent dry conditions. Contrary to sandy soils, only strong rain signals are

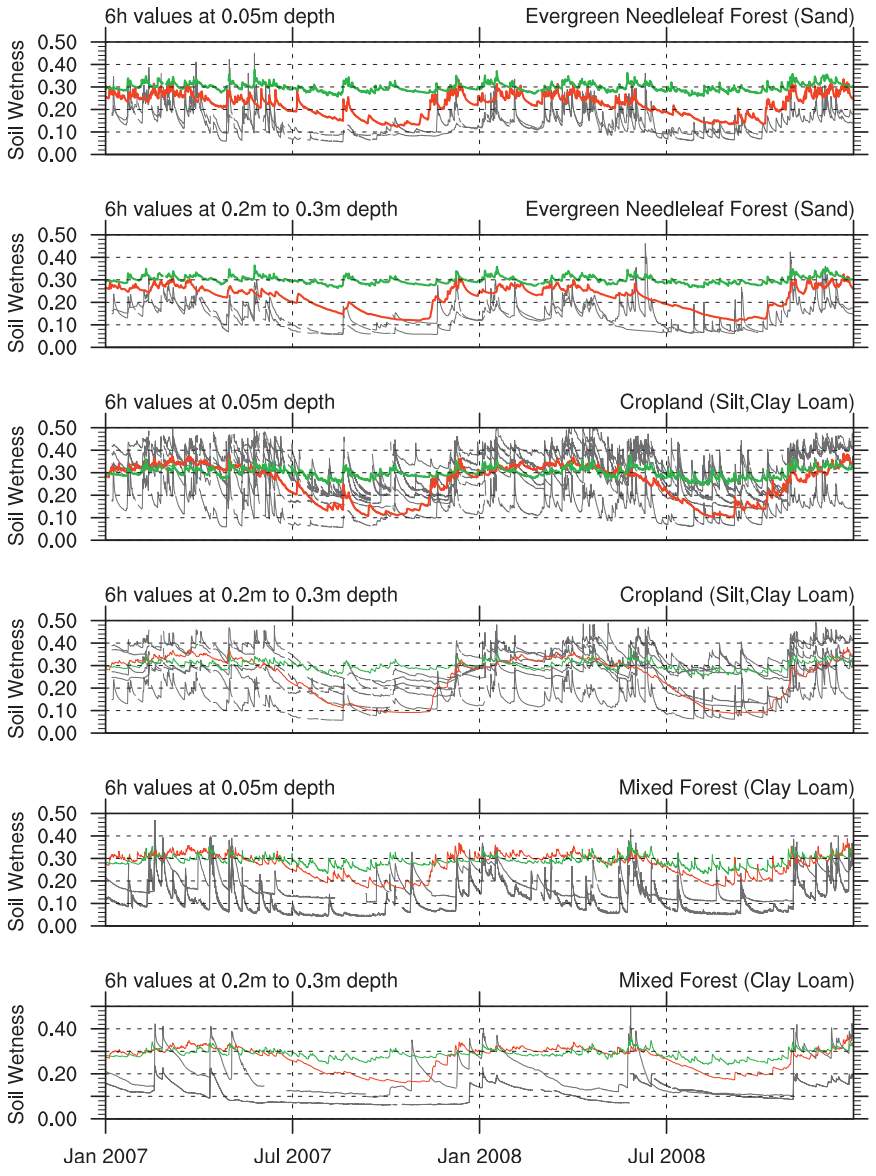


FIG. 4. The 6-hourly soil wetness of those stations within (top two panels) Forêt des Landes, (middle two) cropland, and (bottom two) Mediterranean forest compared with those grid points classified as evergreen needleleaf forest (sand), cropland (clay loam, silt), and mixed forest (clay loam) in WRF-Noah. Areal means are depicted in red for WRF-Noah and in green for ERA-I. SM stations are colored in light gray. For every LUI, both depths (0.05 and 0.25 m) are taken into account. Units are meters cubed per meters cubed.

visible in the deeper soil. Light rain, especially during summer, only alters the soil wetness at 5-cm depth.

These features are neither evident in WRF-Noah nor in ERA-I. Besides low variability on short time scales, those signals corresponding to rain events always propagate into the second layer, although they are become smaller. WRF-Noah once again fails to dry the soil to $\theta_w$. Observations hardly show any seasonal cycle, as the high-frequency variability exceeds those at longer time scales by several orders, whereas in WRF-Noah the seasonal cycle is the most dominant mode of variability.

### *b. Comparison with reanalysis data*

In this section, WRF-Noah is evaluated against ERA-I and CPC. Figure 5 shows seasonal mean SWC of the upper 1.6 m as generated by WRF-Noah. SWC is highest during winter–spring and lowest in summer–autumn. During winter–spring, maximum values range

TABLE 1. Field capacity $\theta_f$ and wilting point $\theta_w$ of the dominant soil categories in the SM domain. ERA-I/TESSEL has a uniform soil texture everywhere.

| Soil texture | $\theta_f$ | $\theta_w$ |
|---|---|---|
| Silt | 0.383 | 0.103 |
| Clay loam | 0.382 | 0.084 |
| Sand | 0.236 | 0.01 |
| Uniform TESSEL | 0.323 | 0.171 |

between 600 and 700 mm and are primarily found in regions with large amounts of precipitation: along the western coastlines of Europe and in the upwind parts of mountainous and alpine regions. In summer–autumn, SWC remains at high values of up to 600 mm in the high-mountain ranges and in northeastern Russia and Scandinavia. The minimum SWC is located, naturally, in the desert regions of northern Africa due to very low annual mean precipitation. Similar values are reached during summer–autumn around the Mediterranean Sea and in eastern Europe, regions with low precipitation and an high evaporative demand during summer. Relative minimums are found in downwind areas of mountain ranges (e.g., the Carpathian Mountains or the Apennines). Very low amounts of SWC occurring in parts of the Sahara (>100 mm) are due to soil classified as bedrock. Sand is always drier relative to its surrounding areas, which is most noticeable for heath

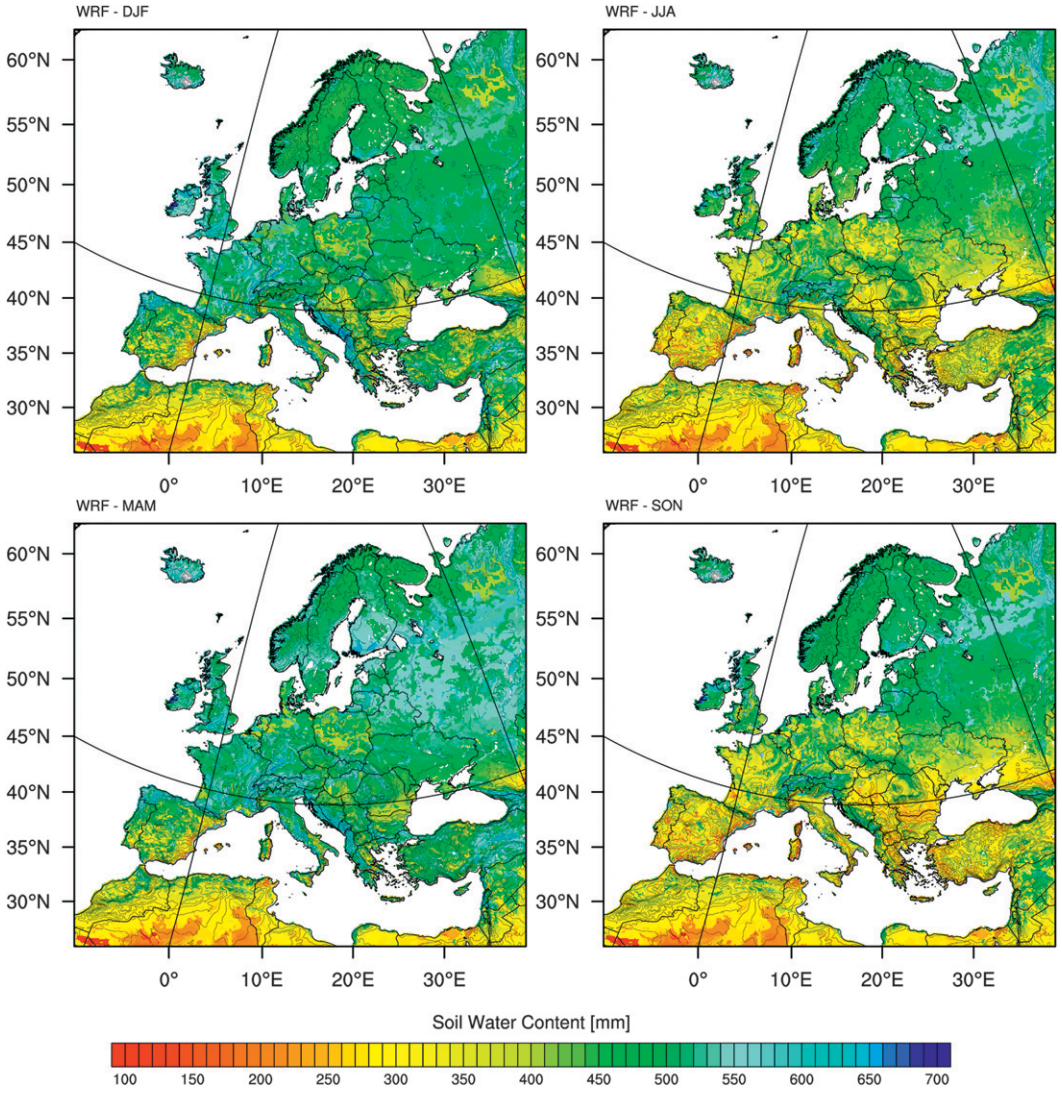


FIG. 5. Seasonal mean SWC of the WRF-Noah Model between 1990 and 2008 for (top left) winter (December–January, DJF), (top right) summer (June–August, JJA), (bottom left) spring (March–May, MAM), and (bottom right) autumn (September–November, SON). The corresponding soil layer depth is 1.6 m (1600 mm).

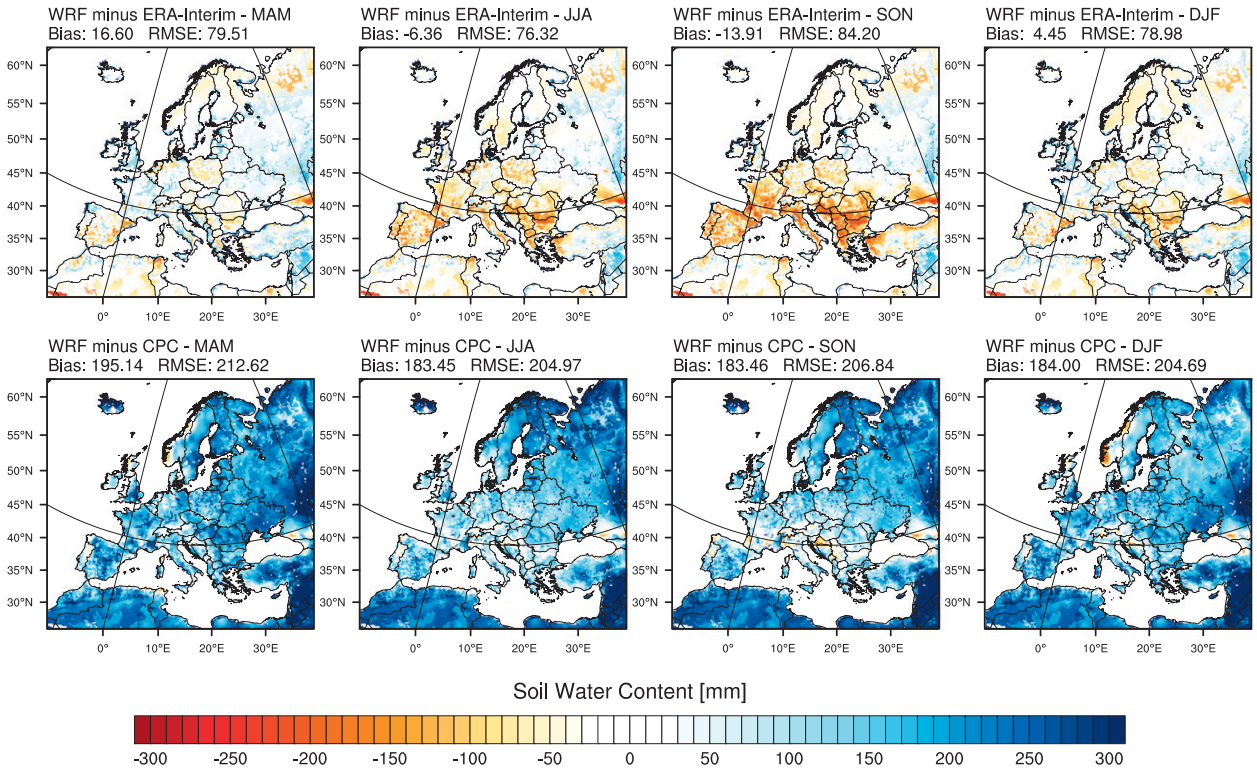


FIG. 6. Difference in seasonal mean SWC (1990–2008) between the WRF-Noah Model and either (top) ERA-I or (bottom) CPC. The corresponding layer depth is 1.6 m (1600 mm). CPC is much drier over most parts of the domain, whereas ERA-I is slightly wetter.

landscapes in central Europe. Silt clay is in general slightly wetter.

Figure 6 reveals the difference when subtracting either ERA-I SWC or CPC SWC from WRF-Noah. According to CPC, WRF-Noah is wetter throughout the year with a mean bias of approximately 184 mm. Differences in central and western Europe range between 100 and 200 mm, which is significantly large. In mountainous regions and along the Atlantic coast, values are near zero. WRF-Noah is drier during wintertime on the upwind side of the Scandinavian Range.

Small biases occur when comparing WRF-Noah with ERA-I over the whole domain. However, on a regional scale, differences are significantly larger. On the Balkans, the Iberian Peninsula, and southern Russia, WRF-Noah is drier during summer. Along the western coastlines and some parts of Russia, WRF-Noah is wetter. WRF-Noah is relatively dry in regions classified as sand (heath landscapes) or loamy sand (Scandinavia), and slightly wetter in those areas classified as sandy loam (northern Russia) or clay loam (e.g., along most river basins).

The standard deviation of the seasonal means gives an impression of interannual variability and is shown in Fig. 7. During winter (Fig. 7, left column), all models show high values in southern Europe, especially in those regions close to the Mediterranean Sea and the subtropical Atlantic Ocean. Standard deviations of CPC in northeastern Europe are large relative to WRF-Noah and ERA-I. Standard deviations show values of approximately 50–70 mm in WRF-Noah and 30–50 mm in ERA-I for southern Europe. Altogether, ERA-I shows the least variability, with values being smaller by more than a factor of 2 than those of WRF-Noah.

During spring, patterns for WRF-Noah and ERA-I change, whereas CPC keeps the same pattern, but with slightly smaller values. Standard deviations in southern Europe decrease for WRF-Noah.

In summer and autumn a band of large standard deviation is located throughout central Europe in WRF-Noah, shifting slightly northward from roughly 40° to 50°N in summer to 45° to 55°N in autumn. In autumn, areas in northern Europe have very low variability. In comparison with ERA-I, patterns are fairly similar, even though ERA-I's variability is roughly 2 times smaller than in WRF-Noah. For CPC, the pattern of variability stays similar to those in winter–spring, but with smaller values. In the far northeastern regions of the domain, variability is relatively small throughout the year.

Standard deviations within a particular season are given in Fig. 8 and reveal intraseasonal variability. As

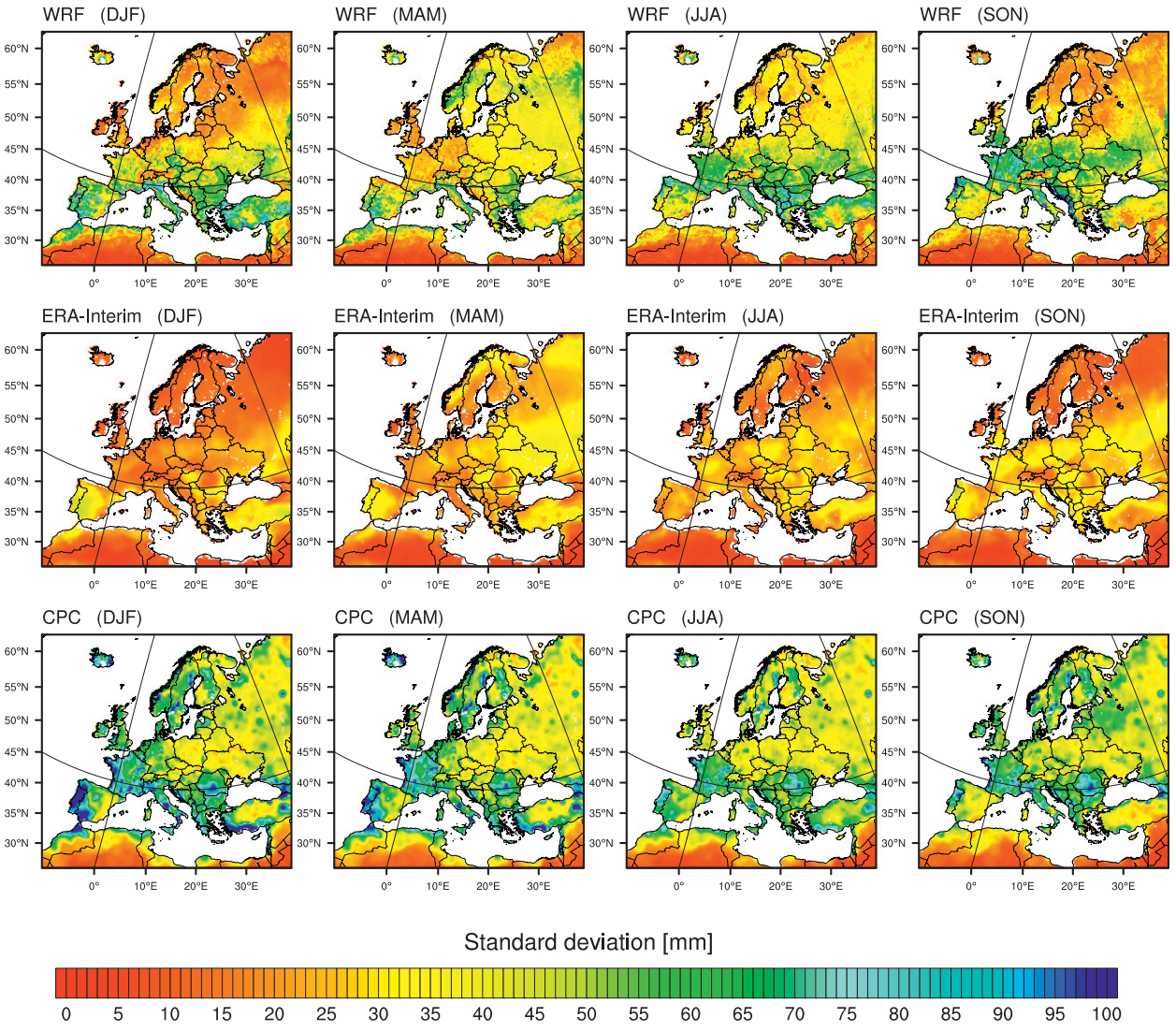


FIG. 7. Standard deviation (mm) of 18 seasonal means of SWC (from 1990 to 2008) for (top) WRF-Noah, (middle) ERA-I, and (bottom) CPC during winter (DJF), spring (MAM), summer (JJA) and autumn (SON). These plots could be interpreted as an interannual variability, which is largest for CPC and lowest for ERA-I.

CPC data are originally given in terms of monthly means, standard deviations have just been computed for WRF-Noah and ERA-I. Intraseasonal variability is approximately 3 times smaller than interannual variability and ERA-I once again shows values 2 times smaller than WRF-Noah.

In winter, areas in northern Europe show nearly no variation in either of the models. In southern Europe, values are high, especially along the northern Mediterranean Sea. In spring, overall, high standard deviations are found in most parts of northern-central and eastern Europe. During autumn, the maximum values of variability are located along the eastern Adriatic coast and in northern Portugal–Spain.

An EOF analysis of the monthly mean SWC in the upper 1.6 m (1600 mm) is shown in Fig. 9. As only trends were removed, the annual cycle is the dominant mode of variability and accounts for roughly 60% of the variance for WRF-Noah, 52% for ERA-I, and 29% for CPC. EOFs of higher order are not considered to be relevant, due to very small explained variances.

Principal component time series of all models are highly correlated ($r_{\text{WRF–ERA}} = 0.92$; $r_{\text{WRF–CPC}} = 0.94$) and negative during winter–spring and positive in summer–autumn. This indicates that in those regions with negative values SWC is higher in winter–spring than in summer autumn. Therefore, areas with large negative values represent areas with distinct differences between wet

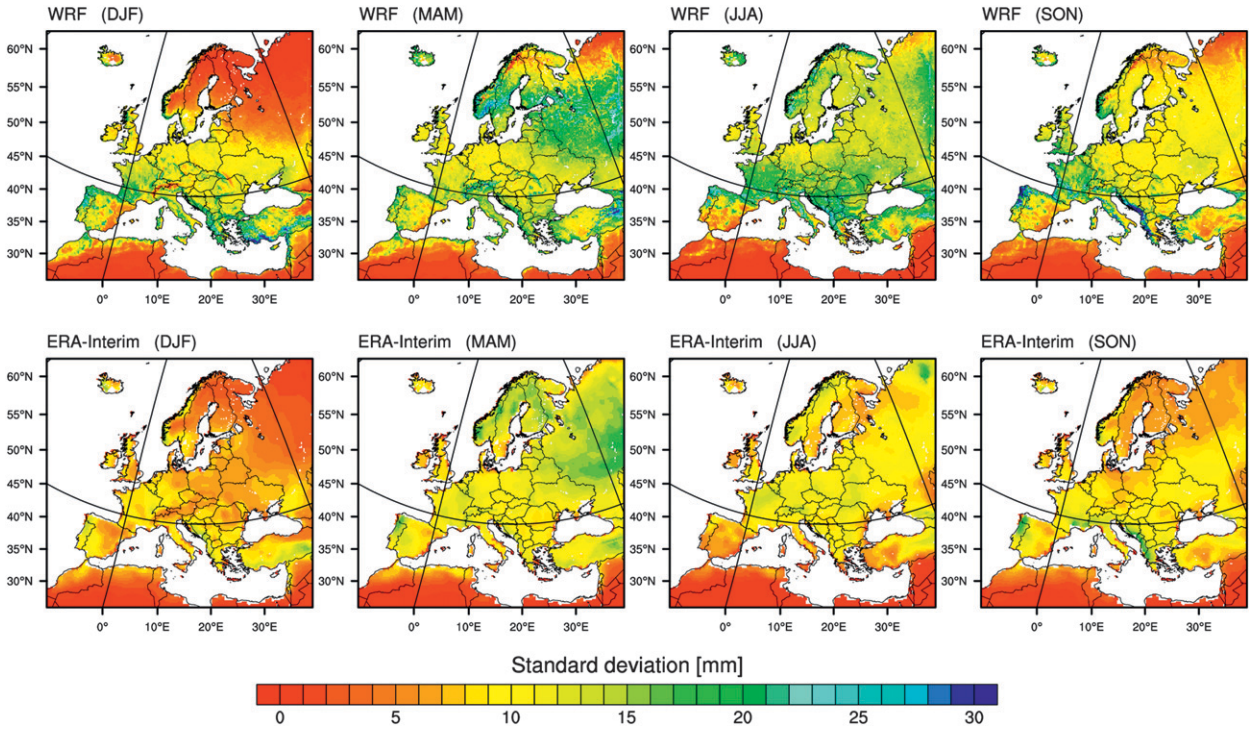


FIG. 8. Mean of 18 seasonal standard deviations (mm) of SWC (from 1990 to 2008) for (top) WRF-Noah and (bottom) ERA-I during winter (DJF), spring (MAM), summer (JJA) and autumn (SON). This could be interpreted as an intraseasonal variability, which is lower in winter as a result of overall wet conditions or extensive snow cover.

and dry conditions in the particular seasons and thus with a strong annual cycle. In general, these regions (western Europe and along the coast of the Mediterranean Sea) are similar for all models. It is important to note the different color bars and *y* axes of the time series. This pattern indicates that the domain-wide variability of ERA-I is lowest, and the strongest annual variations are found for CPC in parts of southern Europe.

In central and eastern Europe, values are less negative in WRF-Noah but still represent a significant annual cycle. When compared with ERA-I, another area of pronounced negative values is found in these areas, especially in the eastern Ukraine and southern Russia. Considering the different *y* axis of the time series, this results in the similar strengths of the annual variability in these regions. Near-zero values are found for WRF-Noah and ERA-I in northern Scandinavia and Russia. This does not necessarily mean that no annual cycle exists at all, but there is no annual cycle with peaks in winter–spring and summer–autumn. For CPC, differences from the other models are large in northern Europe. All models show small values in high-mountain regions.

An EOF analysis after removing the annual cycle from the data (not shown) possibly shows existing superimposed climate modes. For most parameters (e.g., precipitation, sea level pressure, or air temperature) the most important climate mode over Europe is the North Atlantic Oscillation (NAO) (Hurrell 1995; Hurrell and Loon 1997; Visbeck et al. 2001; Keenlyside et al. 2008), which is also important for the variability of hydrologic properties (Shorthouse and Arnell 1999; Trigo et al. 2004). However, this is not evident in any of the models.

## 5. Discussion of the results

Precipitation is the most important input for an LSM. In WRF-Noah and ERA-I, precipitation is generated by the particular atmospheric model. WRF-Noah is likely to generate too large precipitation amounts during winter–spring (Warrach-Sagi et al. 2013). In most parts of Europe precipitation in winter–spring is more likely to be synoptically forced, rather than being convective. Land surface–precipitation feedbacks play only a minor role under these conditions and thus biases in soil wetness are directly related to biases in precipitation. By that reasoning, WRF-Noah's soil wetness is slightly wetter in winter–spring when compared with the observations. ERA-I is much wetter during summer because of artificial increments performed by the data assimilation system and thus fails to capture any of the characteristics of

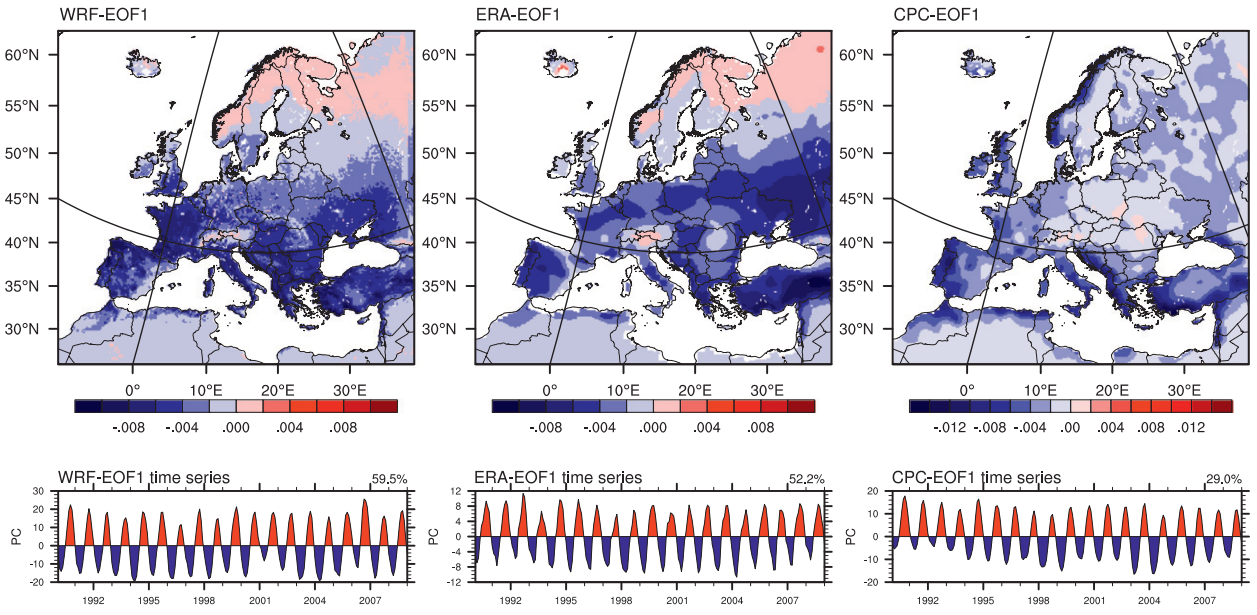


FIG. 9. First EOF of monthly mean SWC in the upper 1.6 m (1600 mm) from 1990 to 2008 from either the (top left) WRF-Noah, (top center) ERA-I, or (top right) CPC with (bottom) the corresponding PC time series. The explained variance (%) is also shown and is high for WRF-Noah and ERA-I. Because just the mean is removed from the data, the dominant variability is the annual cycle with greatest variability in the Mediterranean area. The PC time series are highly correlated ($r_{\mathrm{WRF-ERA}} = 0.91$; $r_{\mathrm{WRF-CPC}} = 0.94$).

the soil hydrology under overall dry conditions. Another factor contributing to the differences between the models is the relatively small available water content (the range between wilting point and field capacity) in ERA-I. WRF-Noah's dominant soil categories show larger available water contents, and thus the soil wetness likely reaches drier values in summer and wetter values in winter. The large layer thickness of 1.6 m also neglects vertical stratification differences, possibly having a large impact in some regions.

Observations further indicate that signals corresponding to rain, lead to very strong and sudden increases in soil wetness. This is caused by high infiltration rates, especially in sandy soils. These signals are weaker in WRF-Noah and are potentially caused by spatial averaging other many grid points and thereby filtering out local rain events occurring at the measurement sites. Infiltration capacity could be underestimated as well. However, due to the uniform soil texture in ERA-I, WRF-Noah is much closer to reality in all three environments.

Those signals induced by rain subsequently decrease relatively fast, due to the combined effects of downward drainage, root water uptake, and surface evaporation. This is especially distinct at the stations in Forêt des Landes, with a rapid drying toward wilting points. This leads to a distinct bimodal structure, which is more continuous for the models. WRF-Noah also dries the soil, only slower, and the soil wetness never reaches the wilting point, which is possibly caused by an insufficient hydraulic conductivity parameterization for sandy soils. This is also evident within the Mediterranean forest. In the cropland environment, WRF-Noah is slightly wetter then SM, possibly caused by an overestimation of evapotranspiration. However, SM shows a large variability for this LUI. Due to soil wetness adjustments in TESSEL, ERA-I always remains at high levels. Within the Mediterranean forest, only strong rain signals are noticeable in the lower layer. This is due to low hydraulic conductivity for clay loam and loam. In WRF-Noah all rain signals spread into the lower layers.

Biases in WRF-Noah to the observations could be separated into systematic biases resulting from inaccurate precipitation input or by insufficient parameterizations of evapotranspiration, drainage, and infiltration capacity. However, WRF-Noah (and with limitations also ERA-I) performs relatively well with respect to the seasonal and intraseasonal variability. To determine the spatial patterns of variability, the analysis was extended to all of Europe for the period from 1990 to 2008. ERA-I and CPC were not assumed to be a reference, as both are models as well. Evaluation of WRF-Noah is thus based on plausibility, if all three models reveal a similar pattern and behavior.

Despite mean differences between WRF-Noah and ERA-I being rather small, they become significant on a regional basis. This issue coincides well with the conclusions of previous studies. Shao and Henderson-Sellers (1996) showed that even if land surface parameters were

adjusted, differences between LSMs can vary by up to 100 mm. Koster et al. (2009) showed that spurious results occur, if one model's SWC is used within a different model. Wei et al. (2010) found that different LSMs produce significantly different climatologies of surface parameters and fluxes. This most possibly results from different input data but can also be influenced by different model physics.

One major limitation of ERA-I is the uniform soil texture. Differences between WRF-Noah and ERA-I occur especially in regions where the soil properties of a certain soil texture differ considerably from those in ERA-Interim. As ERA-I fails to represent important characteristics in the SM domain, WRF-Noah is assumed to provide more realistic results in this case. Physically based downscaling to higher resolutions possibly contributes to this assumption as well.

Another major limitation making ERA-I unsuitable for hydrologic purposes are the increments in the data assimilation system. Especially during summer, ERA-I is by far too wet in southern Europe. Distinctions also occur due to a different grid element representation and LUI fields. Regarding CPC, limiting aspects of the bucket model are the major reason for distinctions from WRF-Noah. As the simplicity of the leaky bucket approach used in CPC, for example, does not allow for extensive snow coverage, differences from the other models are large in northern Europe.

Patterns of interannual and intraseasonal variability are similar for WRF and ERA-I. In spring, melting snow leads to a rapid saturation in parts of northeastern Europe and in the alpine mountain ranges. The onset of snowmelt and also the snow depths and density are different from year to year, resulting in strong interannual variability. WRF-Noah and ERA-I both include snow coverage in their models and thus reproduce this issue fairly well.

In the far northeastern regions, snowmelt and therefore the wettest conditions occur in early summer, which results in a shifted annual cycle. WRF-Noah and ERA-I behave similarly in reflecting such effects.

Especially during summer, but also in autumn, occasionally occurring heavy rain events under overall hot and dry conditions lead to large amounts of water suddenly being infiltrated into the soil. This explains the high intraseasonal variability in most parts of northern-central and eastern Europe. During autumn, the switch from dry summer conditions to winter rain conditions leads to maximum values of variability along the eastern Adriatic coast and in northern Portugal–Spain. In winter, areas with continuous snow cover throughout the season (as in northern Europe) show nearly no variation in either of the models, due to the nonexistent change in frozen SWC beneath a shielding snow cover. In southern Europe, periods of extensive rainfall followed by dry, warm conditions, or vice versa, result in high values of intraseasonal standard deviation.

## 6. Summary and conclusions

The major goal of this study was to evaluate the performance of WRF-Noah against in situ station observations from the SM network in southern France and reanalysis model data provided by ERA-I and CPC.

Evaluation against the in situ measurements was performed within the period from 2007 to 2008. Analyzing the areal mean time series of 12 SM stations reveals that WRF-Noah reflects the annual cycle rather well, but overestimates its amplitude. Larger values in winter appear most probably due to a significant overestimation of precipitation. In summer, SWC is too low. This results possibly from an overestimation of evapotranspiration in a cropland environment, where most SM stations are located. However, those few stations located in Forêt des Landes on sandy soils are significantly drier than is found with WRF-Noah during summer, as evapotranspiration in these areas is possibly underestimated by the model. Similar results are also found for the region of Mediterranean forest, which is classified as mixed forest in WRF-Noah. As mixed forest is also used to classify regions in central and northern Europe with more temperate tree species, the ability of Mediterranean trees to sustain transpiration even under water-limited conditions is not resolved. Introducing more precise vegetation categories may reveal better results.

Evaluations against reanalysis model data show that the patterns of seasonal mean SWC are quite similar, with the highest values during winter–spring in northern-central Europe and the lowest values during summer–autumn in southern Europe. However, the total values differ significantly, whereas WRF-Noah exceeds those of CPC by a large amount. When compared with ERA-I, the largest differences appear during summer–autumn in southern Europe and are negative, indicating that WRF-Noah is drier. Apart from these differences, the patterns of variability are quite similar. If the annual cycle is not removed, it is the most important mode of variability, being largest in southern and western Europe in all models. Noah in WRF and TESSEL in ERA-I are both modern second-generation LSMs and as such treat all aspects related to snow cover and snowmelt similarly. The largest values of SWC appear immediately after snowmelt. However, a globally constant soil texture remains a major limitation of TESSEL.

In summary, WRF-Noah captures the most important factors contributing to the evolution of SWC rather well

and this study shows that differences in the observations and in the other models appear as a consequence of inadequate input data provided by the atmospheric model and insufficient model physics. Comparing large-scale estimates from LSMs with point measurements additionally induces potential errors. It is also evident that dynamical downscaling clearly improves the representation of the soil hydrology. The impacts of such improvements on precipitation and other meteorological parameters need to be investigated in upcoming studies.

However, advancing soil hydrology as introduced, for example, in Zeng and Decker (2009) or Kalinka and Ahrens (2011) and better resolved and distributed soil maps and soil properties (Sanchez et al. 2009; Guillod. et al. 2013) will possibly further improve the results, especially within deeper soils and for runoff simulations (Warrach-Sagi et al. 2008). As the subgrid variability of land surface properties is large and still underrepresented in LSMs, new methods should be developed to account for these issues. The tiled approach, used in TESSEL and in many modern LSMs, is a first step toward this goal. The relevance of an improved treatment of surface runoff is also underlined in Decharme (2007). Furthermore, the need to improve the simulation of root water uptake and transpiration of plants is pointed out by Gayler et al. (2013) and Wöhling et al. (2012). Revised LAI dynamics in croplands will further advance the representation of evapotranspiration, as shown in Ingwersen et al. (2011). Considering additional groundwater fluxes, which are not assumed in most LSMs, is suggested in Maxwell and Miller (2005). LSMs are also improved by surface hydrology data assimilation. Promising results have been achieved recently by using river gauge and discharge measurements, having a high accuracy, to assimilate SWC in the root zone (Pauwels and Lannoy 2006; Warrach-Sagi and Wulfmeyer 2010). In the future, data assimilation of observations will be an important tool for climate simulations, because mesoscale reanalysis with better initialization of land surface and atmospheric fields will permit a more thorough investigation of process understanding and feedback processes. Research into these combined effects requires a considerable community-wide effort, as is ongoing in the Water–Earth System Science (WESS) Competence Center [see Grathwohl et al. (2013) and online at www.wess.info], and the study of catchments as organized systems [see Zehe et al. (2012, manuscript submitted to *Environ. Earth Sci.*) and online at www.caos-project.de].

*Acknowledgments.* The authors thank the German Science Foundation (DFG) for funding this work within the Project DFG-PAK 346/FOR 1695 ''Regional Climate Change'' by the German Science Foundation The authors thank the HLRS staff for the permission and support of the simulations on the High Performance Computer in Stuttgart. The simulations were carried out in collaboration with the Water and Earth System Science (WESS) Consortium funded by the BMBF and UFZ Leipzig. The authors thank the reviewers for their valuable comments.

## REFERENCES

Albergel, C., and Coauthors, 2008: From near-surface to root-zone soil moisture using an exponential filter: An assessment of the method based on in-situ observations and model simulations. *Hydrol. Earth Syst. Sci. Discuss.,* **5,** 1603–1640, doi:10.5194/hessd-5-1603-2008.

Alfieri, L., P. Claps, P. D'Odorico, F. Laio, and T. Over, 2008: An analysis of the soil moisture feedback on convective and stratiform precipitation. *J. Hydrometeor.,* **9,** 280–291.

Barthlott, C., C. Hauck, G. Schädler, N. Kalthoff, and C. Kottmeier, 2011: Soil moisture impacts on convective indices and precipitation over complex terrain. *Meteor. Z.,* **20,** 185–197, doi:10.1127/0941-2948/2011/0216.

Beljaars, A., M. Miller, and P. Viterbo, 1996: The land surface–atmosphere interaction: A review based on observational and global modeling perspectives. *J. Geophys. Res.,* **101,** 7209–7225.

Beniston, M., 2004: The 2003 heat wave in Europe: A shape of things to come? An analysis based on Swiss climatological data and model simulations. *Geophys. Res. Lett.,* **31,** L02202, doi:10.1029/2003GL018857.

Black, E., M. Blackburn, G. Harrison, B. Hoskins, and J. Methven, 2004: Factors contributing to the summer 2003 European heatwave. *Weather,* **59,** 217–223, doi:10.1256/wea.74.04.

Calvet, J., N. Fritz, F. Froissard, D. Suquia, A. Petitpa, and B. Piguet, 2007: In situ soil moisture observations for the CAL/VAL of SMOS: The SMOSMANIA network. *Proc. Int. Geoscience and Remote Sensing Symp.,* Barcelona, Spain, IEEE, 1196–1199.

Chen, F., and J. Dudhia, 2001: Coupling an advanced land surface–hydrology model with the Penn State–NCAR MM5 modeling system. Part I: Model implementation and sensitivity. *Mon. Wea. Rev.,* **129,** 569–585.

Clark, R., S. Brown, and J. Murphy, 2006: Modeling Northern Hemisphere summer heat extreme changes and their uncertainties using a physics ensemble of climate sensitivity experiments. *J. Climate,* **19,** 4418–4435.

Collins, W., and Coauthors, 2004: Description of the NCAR Community Atmosphere Model (CAM 3.0). NCAR Tech. Note NCAR/TN-464+STR, 214 pp.

Decharme, B., 2007: Influence of runoff parameterization on continental hydrology: Comparison between the Noah and the ISBA land surface models. *J. Geophys. Res.,* **112,** D19108, doi:10.1029/2007JD008463.

Dee, D., and Coauthors, 2011: The ERA-Interim reanalysis: Configuration and performance of the data assimilation system. *Quart. J. Roy. Meteor. Soc.,* **137,** 553–597, doi:10.1002/qj.828.

Ek, M., and L. Mahrt, 1994: Daytime evolution of relative humidity at the boundary layer top. *Mon. Wea. Rev.,* **122,** 2709–2721.

——, and A. Holtslag, 2004: Influence of soil moisture on boundary layer cloud development. *J. Hydrometeor.,* **5,** 86–99.

——, K. E. Mitchell, Y. Lin, E. Rogers, P. Grunmann, V. Koren, G. Gayno, and J. D. Tarpley, 2003: Implementation of Noah land surface model advances in the National Centers for

Environmental Prediction operational mesoscale Eta Model. *J. Geophys. Res.,* **108,** 8851, doi:10.1029/2002JD003296.

Eltahir, E., 1998: A soil moisture–rainfall feedback mechanism. 1: Theory and observations. *Water Resour. Res.,* **34,** 765–776.

Fan, Y., H. Van den Dool, D. Lohmann, and K. Mitchell, 2006: 1948–98 U.S. hydrological reanalysis by the Noah land data assimilation system. *J. Climate,* **19,** 1214–1237.

Findell, K., and E. Eltahir, 2003: Atmospheric controls on soil moisture-boundary layer interactions. Part I: Framework development. *J. Hydrometeor.,* **4,** 552–569.

Fischer, E., S. Seneviratne, P. Vidale, D. Lüthi, and C. Schär, 2007: Soil moisture–atmosphere interactions during the 2003 European summer heat wave. *J. Climate,* **20,** 5081–5099.

Gantner, L., and N. Kalthoff, 2010: Sensitivity of a modelled life cycle of a mesoscale convective system to soil conditions over West Africa. *Quart. J. Roy. Meteor. Soc.,* **136** (S1), 471–482, doi:10.1002/qj.425.

Gayler, S., J. Ingwersen, E. Priesack, T. Wöhling, V. Wulfmeyer, and T. Streck, 2013: Assessing the relevance of subsurface processes for the simulation of evapotranspiration and soil moisture dynamics with CLM3.5: Comparison with field data and crop model simulations. *Environ. Earth Sci.,* **69,** 415–427.

Grathwohl, P., and Coauthors, 2013: Catchments as reactors: A comprehensive approach for water fluxes and solute turnover. *Environ. Earth Sci.,* **69,** 317–333.

Guillod, B., E. Davin, C. Kündig, G. Smiatek, and S. Seneviratne, 2013: Impact of soil map specifications for European climate simulations. *Climate Dyn.,* **40,** 123–141, doi:10.1007/s00382-012-1395-z.

Hauck, C., C. Barthlott, L. Krauss, and N. Kalthoff, 2011: Soil moisture variability and its influence on convective precipitation over complex terrain. *Quart. J. Roy. Meteor. Soc.,* **137,** 42–56, doi:10.1002/qj.766.

Heerwaarden, C. V., J. V.-G. de Arellano, A. Moene, and A. Holtslag, 2009: Interactions between dry-air entrainment, surface evaporation and convective boundary-layer development. *Quart. J. Roy. Meteor. Soc.,* **135,** 1277–1291, doi:10.1002/qj.431.

Heikkilä, U., A. Sandvik, and A. Sorteberg, 2011: Dynamical downscaling of ERA-40 in complex terrain using the WRF regional climate model. *Climate Dyn.,* **37,** 1551–1564.

Hirschi, M., and Coauthors, 2010: Observational evidence for soil-moisture impact on hot extremes in southeastern Europe. *Nat. Geosci.,* **4,** 17–21, doi:10.1038/ngeo1032.

Hohenegger, C., P. Brockhaus, C. Bretherton, and C. Schär, 2009: The soil moisture–precipitation feedback in simulations with explicit and parameterized convection. *J. Climate,* **22,** 5003–5020.

Hong, S., Y. Noh, and J. Dudhia, 2006: A new vertical diffusion package with an explicit treatment of entrainment processes. *Mon. Wea. Rev.,* **134,** 2318–2341.

Hurrell, J., 1995: Decadal trends in the North Atlantic Oscillation: Regional temperatures and precipitation. *Science,* **269,** 676–679.

——, and H. van Loon, 1997: Decadal variations in climate associated with the North Atlantic Oscillation. *Climatic Change,* **36,** 301–326.

Ingwersen, J., and Coauthors, 2011: Comparison of noah simulations with eddy covariance and soil water measurements at a winter wheat stand. *Agric. For. Meteor.,* **151,** 345–355, doi:10.1016/j.agrformet.2010.11.010.

Kain, J., 2004: The Kain–Fritsch convective parameterization: An update. *J. Appl. Meteor.,* **43,** 170–181.

Kalinka, F., and B. Ahrens, 2011: A modification of the mixed form of Richards equation and its application in vertically inhomogeneous soils. *Adv. Sci. Res.,* **6,** 123–127, doi:10.5194/asr-6-123-2011.

Kalthoff, N., and Coauthors, 2011: The dependence of convection-related parameters on surface and boundary-layer conditions over complex terrain. *Quart. J. Roy. Meteor. Soc.,* **137,** 70–80, doi:10.1002/qj.686.

Keenlyside, N., M. Latif, J. Jungclaus, L. Kornblueh, and E. Roeckner, 2008: Advancing decadal-scale climate prediction in the North Atlantic sector. *Nature,* **453,** 84–88, doi:10.1038/nature06921.

Koster, R., and Coauthors, 2004: Regions of strong coupling between soil moisture and precipitation. *Science,* **305,** 1138–1140, doi:10.1126/science.1100217.

——, Z. Guo, R. Yang, P. Dirmeyer, K. Mitchell, and M. Puma, 2009: On the nature of soil moisture in land surface models. *J. Climate,* **22,** 4322–4335.

Lorenz, R., E. Jaeger, and S. Seneviratne, 2010: Persistence of heat waves and its link to soil moisture memory. *Geophys. Res. Lett.,* **37,** L09703, doi:10.1029/2010GL042764.

Mahfouf, J., P. Viterbo, H. Douville, A. Beljaars, and S. Saarinen, 2000: A revised land-surface analysis scheme in the integrated forecasting system. *ECMWF Newsletter,* No. 88, ECMWF, Reading, United Kingdom, 8–13.

Mahrt, L., and M. Ek, 1984: The influence of atmospheric stability on potential evaporation. *J. Climate Appl. Meteor.,* **23,** 222–234.

Manabe, S., and K. Bryan, 1969: Climate calculations with a combined ocean–atmosphere model. *J. Atmos. Sci.,* **26,** 786–789.

Maxwell, R., and N. Miller, 2005: Development of a coupled land surface and groundwater model. *J. Hydrometeor.,* **6,** 233–247.

Morrison, H., G. Thompson, and V. Tatarskii, 2009: Impact of cloud microphysics on the development of trailing stratiform precipitation in a simulated squall line: Comparison of one- and two-moment schemes. *Mon. Wea. Rev.,* **137,** 991–1007.

Pauwels, V., and G. D. Lannoy, 2006: Improvement of modeled soil wetness conditions and turbulent fluxes through the assimilation of observed discharge. *J. Hydrometeor.,* **7,** 458–477.

Sanchez, P., and Coauthors, 2009: Digital soil map of the world. *Science,* **325,** 680–681, doi:10.1126/science.1175084.

Santanello, J., M. Friedl, and M. Ek, 2007: Convective planetary boundary layer interactions with the land surface at diurnal time scales: Diagnostics and feedbacks. *J. Hydrometeor.,* **8,** 1082–1097.

Schär, C., D. Lüthi, U. Beyerle, and E. Heise, 1999: The soil–precipitation feedback: A process study with a regional climate model. *J. Climate,* **12,** 722–741.

Schwitalla, T., H. Bauer, V. Wulfmeyer, and F. Aoshima, 2011: High-resolution simulation over central Europe: Assimilation experiments during COPS IOP 9C. *Quart. J. Roy. Meteor. Soc.,* **137** (S1), 156–175, doi:10.1002/qj.721.

Sellers, P., and Coauthors, 1997: Modeling the exchanges of energy, water, and carbon between continents and the atmosphere. *Science,* **275,** 502–509, doi:10.1126/science.275.5299.502.

Seneviratne, S., D. Lüthi, M. Litschi, and C. Schär, 2006: Land–atmosphere coupling and climate change in Europe. *Nature,* **443,** 205–209, doi:10.1038/nature05095.

——, T. Corti, E. Davin, M. Hirschi, E. Jaeger, I. Lehner, B. Orlowsky, and A. Teuling, 2010: Investigating soil moisture–climate interactions in a changing climate: A review. *Earth Sci. Rev.,* **99,** 125–161, doi:10.1016/j.earscirev.2010.02.004.

Shao, Y., and A. Henderson-Sellers, 1996: Modeling soil moisture: A Project for Intercomparison of Land Surface

Parameterization Schemes phase 2(B). *J. Geophys. Res.,* **101** (D3), 7227–7250.

Shorthouse, C., and N. Arnell, 1999: The effects of climatic variability on spatial characteristics of European river flows. *Phys. Chem. Earth,* **24B,** 7–13.

Skamarock, W., and Coauthors, 2008: A description of the Advanced Research WRF version 3. NCAR Tech. Note NCAR/TN-475+STR, 113 pp.

Taylor, C., and R. Ellis, 2006: Satellite detection of soil moisture impacts on convection at the mesoscale. *Geophys. Res. Lett.,* **33,** L03404, doi:10.1029/2005GL025252.

Trigo, R., D. Pozo-Vázquez, T. Osborn, Y. Castro-Díez, S. Gámiz-Fortis, and M. Esteban-Parra, 2004: North Atlantic Oscillation influence on precipitation, river flow and water resources in the Iberian Peninsula. *Int. J. Climatol.,* **24,** 925–944, doi:10.1002/joc.1048.

Van den Dool, H., J. Huang, and Y. Fan, 2003: Performance and analysis of the constructed analogue method applied to U.S. soil moisture over 1981–2001. *J. Geophys. Res.,* **108,** 8617, doi:10.1029/2002JD003114.

Visbeck, M., J. Hurrell, L. Polvani, and H. Cullen, 2001: The North Atlantic Oscillation: Past, present, and future. *Proc. Natl. Acad. Sci. USA,* **98,** 12 876–12 877, doi:10.1073/pnas.231391598.

Viterbo, P., and A. Beljaars, 1995: An improved land surface parameterization scheme in the ECMWF model and its validation. *J. Climate,* **8,** 2716–2748.

Warrach, K., H.-T. Mengelkamp, and E. Raschke, 2001: Treatment of frozen soil and snow cover in the land surface model SEWAB. *Theor. Appl. Climatol.,* **69,** 23–37.

Warrach-Sagi, K., and V. Wulfmeyer, 2010: Streamflow data assimilation for soil moisture analysis. *Geosci. Model Dev.,* **3,** 1–12, doi:10.5194/gmdd-2-551-2009.

——, ——, R. Grasselt, F. Ament, and C. Simmer, 2008: Streamflow simulations reveal the impact of the soil parameterization. *Meteor. Z.,* **17,** 751–762, doi:10.1127/0941-2948/2008/0343.

——, T. Schwitalla, V. Wulfmeyer, and H.-S. Bauer, 2013: Evaluation of a simulation based on the WRF-Noah model system: Precipitation in Germany. *Climate Dyn.,* **41,** 755–774.

Wei, J., P. Dirmeyer, Z. Guo, L. Zhang, and V. Misra, 2010: How much do different land models matter for climate simulation? Part I: Climatology and variability. *J. Climate,* **23,** 3120–3134.

Wöhling, T., S. Gayler, J. Ingwersen, T. Streck, J. Vrugt, and E. Priesack, 2012: Multiobjective calibration of coupled soil-vegetation-atmosphere models. *Proc. ModelCARE2011: Models—Repositories of Knowledge*. S. E. Oswald, O. Kolditz, and S. Attinger, Eds. Publ. 255, IAHS, 357–364.

Wood, E., and Coauthors, 1998: The Project for Intercomparison of Land-surface Parameterization Schemes (PILPS) Phase 2(c) Red–Arkansas River basin experiment: 1. Experiment description and summary intercomparisons. *Global Planet. Change,* **19,** 115–135, doi:10.1016/S0921-8181(98)00044-7.

Wulfmeyer, V., and Coauthors, 2011: The Convective and Orographically-induced Precipitation Study (COPS): The scientific strategy, the field phase, and research highlights. *Quart. J. Roy. Meteor. Soc.,* **137** (S1), 3–30, doi:10.1002/qj.752.

Yeh, T., R. Wetherald, and S. Manabe, 1984: The effect of soil moisture on the short-term climate and hydrology change—A numerical experiment. *Mon. Wea. Rev.,* **112,** 474–490.

Zeng, X., and M. Decker, 2009: Improving the numerical solution of soil moisture–based Richards equation for land models with a deep or shallow water table. *J. Hydrometeor.,* **10,** 308–319.